Fluid-structure interaction of three-dimensional magnetic artificial cilia

Khaderi, S. N.; Onck, P. R.

Link to publication in University of Groningen/UMCG research database

Fluid–structure interaction of three-dimensional magnetic artificial cilia

S. N. Khaderi and P. R. Onck†

Zernike Institute for Advanced Materials, University of Groningen, 9747 AG Groningen, The Netherlands

A numerical model is developed to analyse the interaction of artificial cilia with the surrounding fluid in a three-dimensional setting in the limit of vanishing fluid inertia forces. The cilia are modelled using finite shell elements and the fluid is modelled using a boundary element approach. The coupling between both models is performed by imposing no-slip boundary conditions on the surface of the cilia. The performance of the model is verified using various reference problems available in the literature. The model is used to simulate the fluid flow due to magnetically actuated artificial cilia. The results show that narrow and closely spaced cilia create the largest flow, that metachronal waves along the width of the cilia create a significant flow in the direction of the cilia width and that the recovery stroke in the case of the out-of-plane actuation of the cilia strongly depends on the cilia width.

Key words: low-Reynolds-number flows, microfluidics, propulsion

---

1. Introduction

Lab-on-a-chip is a field that aims at performing chip-based biochemical assays on small volumes of fluids. A typical lab-on-a-chip has different microchambers for fluidic input, mixing, incubation and biochemical analysis. The test fluid has to be passed through microchannels that connect different chambers. One of the main challenges in the design of microfluidic/lab-on-a-chip systems is the propulsion of fluids through these channels. Researchers have developed propulsion systems which range from externally driven syringe pumps to internally operating electro-osmotic pumps (Laser & Santiago 2004). Recently, much attention has been focused on designing microfluidic propulsion systems by mimicking fluid propulsion mechanisms available in nature (den Toonder *et al.* 2008; Fahrni, Prins & van IJzendoorn 2009; Gauger, Downton & Stark 2009; van Oosten, Bastiaansen & Broer 2009). An example of natural propulsion mechanisms is the expulsion of mucus from the lungs due to hair-like structures, called cilia, that cover the inner layer of the mammalian trachea (Fulford & Blake 1986). The cilia beat back and forth in an asymmetric manner with an effective stroke and a recovery stroke. They propel a relatively larger volume of fluid during the effective stroke when compared with the recovery stroke, and therefore create a net fluid transport in the direction of the effective stroke. Using a two-dimensional numerical model it was shown that thin magnetic films can mimic the beat motion of natural cilia when subjected to a tuned external magnetic field

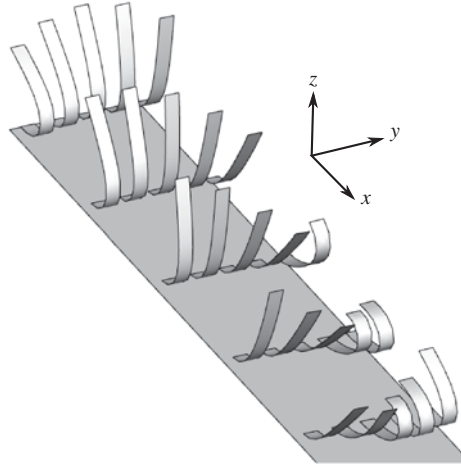† Email address for correspondence: p.r.onck@rug.nl

FIGURE 1. Schematic description of the problem: a group of cilia in a semi-infinite fluid are attached to a substrate and actuated using an external magnetic field.

(Khaderi *et al.* 2009). In a similar fashion, plate-like magnetic artificial cilia have also been synthesized and integrated in microfluidic systems to manipulate fluids (Fahrni *et al.* 2009; Belardi *et al.* 2011; Hussong *et al.* 2011; Khaderi *et al.* 2011*a*). The two-dimensional analysis is valid for cilia widths that are larger than the cilia length and channel height. However, the synthesized cilia are, in general, three-dimensional structures and have a finite width (typically one fifth of their length) Khaderi *et al.* (2011*a*), see figure 1. In these situations, the effect of the cilia width and the spacing between the cilia along the width direction play an important role in determining the fluid transported. In addition, in experimental systems the magnetic field can be applied in three spatial directions. In order to model these effects we develop a three-dimensional numerical model which can accurately describe the motion of the cilia, the velocity field in the fluid and the magnetic field in the cilia, for the situation of low Reynolds numbers.

   To capture the deformation of the cilia, both the bending and membrane stiffnesses (stiffness associated with the in-plane stretching of the cilia) have to be accurately modelled. To do so, we adopt the approach proposed by Bathe & Ho (1981) and model the bending of the cilia using discrete Kirchhoff triangles (DKTs), while the membrane behaviour is accounted for using constant strain triangles (CSTs). To improve the accuracy during in-plane bending, we add drilling degrees of freedom to the CSTs (Allman 1984). The large deformation of the cilia is modelled by adopting an updated Lagrangian procedure.

   We assume that the inertia forces in the fluid are negligible. This enables us to model the fluid using the Stokes equation, the solution of which can be written in terms of a Green's function. The Green's function for the case of forces acting in a semi-infinite fluid is provided by Blake (1971). The cilia are considered as internal boundaries to the fluid, which exert a force on the fluid. The drag forces are treated as a distribution of point forces on the cilia. Akin to the solid mechanics model, we use triangular elements to discretize the internal fluid boundary. The drag forces are assumed to vary linearly within each triangular element. Once the drag traction is

known, the velocity field in the fluid and the velocity of the internal fluid boundary (the cilia) can be obtained.

Many studies exist in the literature to model the interaction of slender bodies with the surrounding fluid, such as the arbitrary Lagrangian–Eulerian (ALE) method (Donea, Giuliani & Halleux 1982), fictitious domain method (van Loon, Anderson & van de Vosse 2006) and immersed boundary method (Peskin 2002). Recently, the extended finite-element method has also been used to perform fluid–structure interaction (FSI) (Gerstenberger & Wall 2008, 2010). Although implementation of these methods for three-dimensional problems is straightforward, the computational cost is enormous due to the large number of degrees of freedom of the three-dimensional fluid mesh. Therefore, coupling a boundary element model of the fluid with a finite-element model of a slender structure provides attractive advantages. Coupling of boundary elements and finite elements has been performed in the past for the interaction of a solid with an ideal fluid (Chen, Hofstetter & Mang 1998; Schneider 2008). In this work we couple the previously explained boundary element formulation for the fluid with the shell element model of the cilia using no-slip boundary conditions on the cilia (the velocity of the fluid boundary is equal to the velocity of the solid shell structure). The coupling is performed in a monolithic fashion. An approach similar to that taken here was used by Salsac, Biesel & Tallec (2010), where the solid–fluid coupling is implemented in an explicit manner. The developed model is used to study: (i) the effect of non-uniformity of the cilia width on the cilia motion and the related flow; (ii) the effect of cilia width and spacing on the fluid transported; and (iii) the effect of laeoplectic metachronal waves and three-dimensional out-of-plane motion of the cilia.

The paper is organized as follows. In §2 we discuss the solid mechanics model followed by the fluid dynamics model and the FSI implementation. The method used to calculate the magnetic fields is then discussed. The results are presented in §3. Several benchmark tests are included in the appendices B–E to verify the numerical accuracy of the proposed model.

2. Formulation

2.1. *Solid mechanics model*

The cilia are modelled using shell elements based on the superposition of the bending and membrane stiffness in the local coordinate axes of the shell element. The membrane stiffness is based on constant strain triangles with drilling degrees of freedom (Allman 1984), and the bending stiffness is based on the discrete Kirchhoff triangular elements proposed by Batoz, Bathe & Ho (1980). We start with the principle of virtual work containing the relevant energies, linearize it, and finally adopt an updated Lagrangian framework to arrive at the final set of equations. The resulting stiffness matrix includes the geometric nonlinearity, which accounts for large deformations, but small strains. In the following, we briefly present the solid mechanics model. The details are provided in appendix A.

Let the displacement of a point on the mid-surface be (u_0, v_0, w_0). As we model the cilia to be shell structures, the displacement of any point on the normal is

$$u = u_0 + z\beta_x, \quad v = v_0 - z\beta_y, \quad w = w_0, \tag{2.1}$$

where β_x and β_y are the rotations of the normal with respect to the x and y axes, respectively. The internal virtual work is

$$\delta W_{int} = \int_{V_0} (\sigma_x \delta\epsilon_x + \sigma_y \delta\epsilon_y + 2\sigma_{xy} \delta\epsilon_{xy}) \, dV_0, \tag{2.2}$$

where σ_x, σ_y and σ_{xy} are the components of the second Piola–Kichhoff stress tensor, ϵ_x, ϵ_y and ϵ_{xy} are the components of the Green–Lagrange strain tensor and dV_0 represents an elemental volume in the undeformed configuration. The internal virtual work after linearization and discretization can be written as (see (A 22))

$$\delta W_{int}^{t+\Delta t} = \delta \boldsymbol{P}^{\mathrm{T}} \boldsymbol{F}_{int}^{t} + \delta \boldsymbol{P}^{\mathrm{T}} (\boldsymbol{K_M} + \boldsymbol{K_G}) \Delta \boldsymbol{P}, \tag{2.3}$$

where $\boldsymbol{P}$ is the global displacement vector, $\boldsymbol{K_M}$ is the material stiffness matrix, $\boldsymbol{K_G}$ is the geometric stiffness matrix and $\boldsymbol{F}_{int}^{t}$ is the internal force vector at time t.

The external work at time $t + \Delta t$ due to body forces and body moments can be written as

$$\delta W_{ext}^{t+\Delta t} = \int_V (f_x \delta u + f_y \delta v + f_z \delta w - N_x \delta \beta_y + N_y \delta \beta_x) \, dV, \tag{2.4}$$

where f_x, f_y and f_z are the body forces and N_x and N_y are the body moments. After discretizing, the external virtual work can be written as (see (A 26))

$$\delta W_{ext}^{t+\Delta t} = \delta \boldsymbol{P}^{\mathrm{T}} \boldsymbol{F}_{ext}^{t+\Delta t}. \tag{2.5}$$

2.2. *Fluid dynamics model*

To model the fluid we use the boundary element method. The cilia, which are immersed in the fluid and fixed to a substrate, exert forces on the fluid. The velocity $\boldsymbol{u}^f$ at a point in the fluid $\boldsymbol{r}$ due to a point force exerted on the fluid by the cilia at a position $\boldsymbol{r}'$ can be obtained using Green's function as

$$\boldsymbol{u}^f(\boldsymbol{r}) = \boldsymbol{G}(\boldsymbol{r}, \boldsymbol{r}', d(\boldsymbol{r}')) \boldsymbol{f}(\boldsymbol{r}'), \tag{2.6}$$

with $d(\boldsymbol{r}')$ being the distance of the point force from the substrate. The Green's function $\boldsymbol{G}(\boldsymbol{r}, \boldsymbol{r}', d(\boldsymbol{r}'))$ for a point force $\boldsymbol{f}(\boldsymbol{r}')$ acting in a fluid near a no-slip boundary is given by Blake (1971). We assume that this point force is distributed over the boundary of the cilia S as a traction $\boldsymbol{t}^f(\boldsymbol{r}')$, where $\boldsymbol{r}'$ is a point on S. Now, the velocity in the fluid can be written as

$$\boldsymbol{u}^f(\boldsymbol{r}) = \int_S \boldsymbol{G}(\boldsymbol{r}, \boldsymbol{r}', d(\boldsymbol{r}')) \boldsymbol{t}^f(\boldsymbol{r}') \, dS. \tag{2.7}$$

The cilia surface is discretized using 'nelm' three-node triangular elements,

$$\boldsymbol{u}^f(\boldsymbol{r}) = \sum_{j=1}^{nelm} \int_{S_j} \boldsymbol{G}(\boldsymbol{r}, \boldsymbol{r}^j, d(\boldsymbol{r}^j)) \boldsymbol{t}^f(\boldsymbol{r}^j) \, dS_j, \tag{2.8}$$

where $\boldsymbol{r}^j$ is a point in the triangular element and the tractions $\boldsymbol{t}^f(\boldsymbol{r}^j)$ are assumed to be varying linearly over the element,

$$\boldsymbol{t}^f(\boldsymbol{r}^j) = \boldsymbol{N} [\{t_1^x \ t_1^y \ t_1^z \ 0 \ 0 \ 0 \ t_2^x \ t_2^y \ t_2^z \ 0 \ 0 \ 0 \ t_3^x \ t_3^y \ t_3^z \ 0 \ 0 \ 0\}_j^f]^{\mathrm{T}} = \boldsymbol{N} \boldsymbol{T}_j^f, \tag{2.9}$$

where t_k^l is the traction at the kth node in the lth direction. As (2.8) is valid for all of the nodes on the cilium ($\boldsymbol{r} = \boldsymbol{r}^i$), we get

$$\boldsymbol{u}^f(\boldsymbol{r}^i) = \sum_{j=1}^{nelm} \int_{S_j} \boldsymbol{G}(\boldsymbol{r}^i, \boldsymbol{r}^j, d(\boldsymbol{r}^j)) \boldsymbol{t}^f(\boldsymbol{r}^j) \, dS_j, \tag{2.10a}$$

$$\boldsymbol{u}_i^f = \sum_{j=1}^{nelm} \int \boldsymbol{G}_{ij} \boldsymbol{N} \, dS_j \boldsymbol{T}_j^f, \tag{2.10b}$$

with $\mathbf{G}_{ij} = \mathbf{G}(\mathbf{r}^i, \mathbf{r}^j, d(\mathbf{r}^j))$. Equation (2.10) relates the velocity of the ith node to all tractions exerted by the surface of the cilia on the fluid. The non-singular integrals in (2.10) are evaluated using standard two-dimensional Gaussian quadrature and the singular integrals are evaluated using the method of change of variables (Pozrikidis 2002, p. 120). Equation (2.10) is evaluated at all nodes on the cilia, and the obtained equations are assembled in a matrix $\mathbf{G}$, which relates the traction exerted by the cilia on the fluid to its velocity, $\mathbf{U}^f = \mathbf{G}\mathbf{T}^f$. Once the velocity of the surface is known, this relation can be inverted to obtain the nodal tractions: $\mathbf{T}^f = \mathbf{G}^{-1}\mathbf{U}^f$.

2.3. *Solid–fluid coupling*

The effect of fluid drag is incorporated as an external force to the solid mechanics model, which provides an additional contribution to the external virtual work. The external virtual work at time $t + \Delta t$ on the jth shell element due to the fluid drag is

$$\delta W_{fluid}^{t+\Delta t} = -\int \mathbf{t}_j^f \cdot \delta \mathbf{u} \, \mathrm{d}S = -\int (\delta \mathbf{u} \cdot \mathbf{N}) \, \mathrm{d}S T_j^f \approx -\delta \mathbf{p} \int \mathbf{N}^\mathrm{T} \mathbf{N} \, \mathrm{d}S T_j^f = -\delta \mathbf{p} \mathbf{M}^j \mathbf{T}_j^f, \quad (2.11)$$

where $\mathbf{M}^j = \int \mathbf{N}^\mathrm{T} \mathbf{N} \, \mathrm{d}S$, $\mathbf{u}$ is the displacement vector and $\mathbf{p}$ is the local nodal displacement vector. After performing the standard finite-element assembly procedure we get

$$\delta W_{fluid}^{t+\Delta t} = -\delta \mathbf{P} \mathbf{M} \mathbf{T}^f = -\delta \mathbf{P} \mathbf{M} \mathbf{G}^{-1} \mathbf{U}^f. \quad (2.12)$$

Using the no-slip boundary condition $\mathbf{U}^f = \mathbf{A}\Delta \mathbf{P}/\Delta t$, where $\mathbf{A}$ is a matrix that eliminates the rotational degrees of freedom from the global displacement vector $\Delta \mathbf{P}$, equation (2.12) can be written as

$$\delta W_{fluid}^{t+\Delta t} = -\delta \mathbf{P} \mathbf{M} \mathbf{G}^{-1} \mathbf{A}\Delta \mathbf{P}/\Delta t, = -\delta \mathbf{P}^\mathrm{T} \mathbf{K}_f \Delta \mathbf{P} \quad (2.13)$$

where $\mathbf{K}_f = \mathbf{M} \mathbf{G}^{-1} \mathbf{A}/\Delta t$ is the stiffness contribution due to the presence of the fluid.

Equating the internal (2.3) and the external virtual work (the sum of (2.5) and (2.13)), and invoking the arbitrariness of the virtual displacements, we get the final equation of motion for the FSI problem:

$$(\mathbf{K}_M + \mathbf{K}_G + \mathbf{K}_f)\Delta \mathbf{P} = \mathbf{F}_{ext}^{t+\Delta t} - \mathbf{F}_{int}^t. \quad (2.14)$$

After incorporating the appropriate boundary conditions, equation (2.14) is solved for the displacement increment $\Delta \mathbf{P}$.

2.4. *Magneto-static model*

The cilia are magnetic films which respond to an external magnetic field. The magnetic response of the cilia is characterized by the magnetic susceptibility tensor $\boldsymbol{\chi}$, through the constitutive relation $\mathbf{M} = \boldsymbol{\chi} \mathbf{H}$, where $\mathbf{M}$ is the magnetization and $\mathbf{H}$ is the magnetic field. The magnetic body couple acting on the cilia $\mathbf{N}_c$ is obtained from the cross-product of the magnetization and the magnetic field intensity $\mathbf{N}_c = \mathbf{M} \times \mathbf{B}_{ext}$, where $\mathbf{M}$ is the magnetization and $\mathbf{B}_{ext}$ is the external magnetic field with a magnitude B_{ext}. The magnetization $\mathbf{M}$ has to be found by solving the Maxwell's equations of electromagnetism. However, we adopt a simpler approach and make use of the fact that the cilia are slender enough to not perturb the external magnetic field significantly; the magnetic field just outside the cilia is equal to the applied magnetic field. The magnetic field inside the cilia can be determined from the electromagnetic boundary conditions: $B_z = B_z^{ext}$, $H_x = H_x^{ext}$, $H_y = H_y^{ext}$, where $\mathbf{H}_{ext} = \mathbf{B}_{ext}/\mu_0$, μ_0 is the permeability of free space and x, y and z refer to the local coordinate axes of the shell

element. Using the first boundary condition and the constitutive behaviour we can find the field H_z inside the cilia as

$$H_z = \frac{B_z^{ext} - \mu_0(H_x^{ext}\chi_{xz} + H_y^{ext}\chi_{yz})}{\mu_0(1 + \chi_{zz})}. \tag{2.15}$$

Once the field in the cilia $\boldsymbol{H}$ is determined, the magnetization of the cilia ($\boldsymbol{M} = \chi \boldsymbol{H}$) and the magnetic body couple ($\boldsymbol{N_c}$) can be found, which are applied as external body moments in (2.4). The only assumption made in this approach is that the magnetic field outside the cilia is the external magnetic field, i.e. we neglect the magnetic field caused by the magnetization of cilia.

3. Results

The three-dimensional model is verified through a number of benchmark problems for the solid mechanics model, the fluid dynamics model, the FSI model and the magneto-static model (see appendices B–E). In this section we use the magneto-mechanical model to study the following aspects of super-paramagnetic (SPM) artificial cilia: the effect of non-uniformity of the cilia width on the cilia motion and flow, the effect of finite width of cilia and the spacing in the width direction on the fluid transported and finally, the effect of laeoplectic metachronal waves and the flow due to three-dimensional motion of cilia.

In the cases shown the length L of the cilia is 100 μm and the thickness h is 2 μm. The elastic modulus of the cilia E is 1 MPa, the Poisson's ratio $\nu = 0.0$ and the fluid viscosity μ is 1 mPa s. The magnetic susceptibilities of the cilia are $\chi_{xx} = 4.6$ and $\chi_{yy} = \chi_{zz} = 0.8$ (all other components are taken to be zero). We apply a magnetic field of magnitude $B_{ext} = 20$ mT, rotating about the y-axis with a frequency of 50 Hz. As the cilia are SPM, the cilia complete one beat cycle in $t_{beat} = 10$ ms (Khaderi, den Toonder & Onck 2011b). In the simulations, the fixed edges of the cilia are placed $0.1L$ above the no-slip boundary, to mimic the presence of the sacrificial layer used during the manufacturing process (den Toonder *et al.* 2008; Fahrni *et al.* 2009).

For the magnetic artificial cilia studied in this paper the relevant forces are the bending forces, viscous forces and magnetic forces. Following Khaderi *et al.* (2009), these can be combined to form a set of two dimensionless parameters: the magnetic number $M_n = 12(B_{ext}^2/\mu_0 E)(L/h)^2$, the ratio of magnetic to elastic bending forces, and the fluid number $F_n = 12(\mu/Et_{beat})(L/h)^3$, the ratio of viscous to elastic bending forces. For the values mentioned earlier the dimensionless parameters can be estimated to be $(M_n, F_n) = (9.55, 0.15)$. These dimensionless parameters signify that the magnetic forces are larger and the viscous forces are smaller than the elastic forces.

3.1. *Motion of a cilium with non-uniform width*

Experiments have shown that cilia of uniform width can be manufactured using lithography techniques (Belardi *et al.* 2011). It is of interest to investigate what shapes and cilia spacings create maximum fluid transport. To this end we first study the motion of one cilium whose width decreases linearly from the fixed end to the free end. To quantify the amount of non-uniformity (tapering) in the width, we define the geometric parameter $T = (b - b_1)/b$, where b and b_1 are the widths of cilium at the fixed and the free edges, respectively. The width of the cilium at the fixed edge is taken to be $L/10$. When T is zero the cilium has uniform width; whereas the cilium
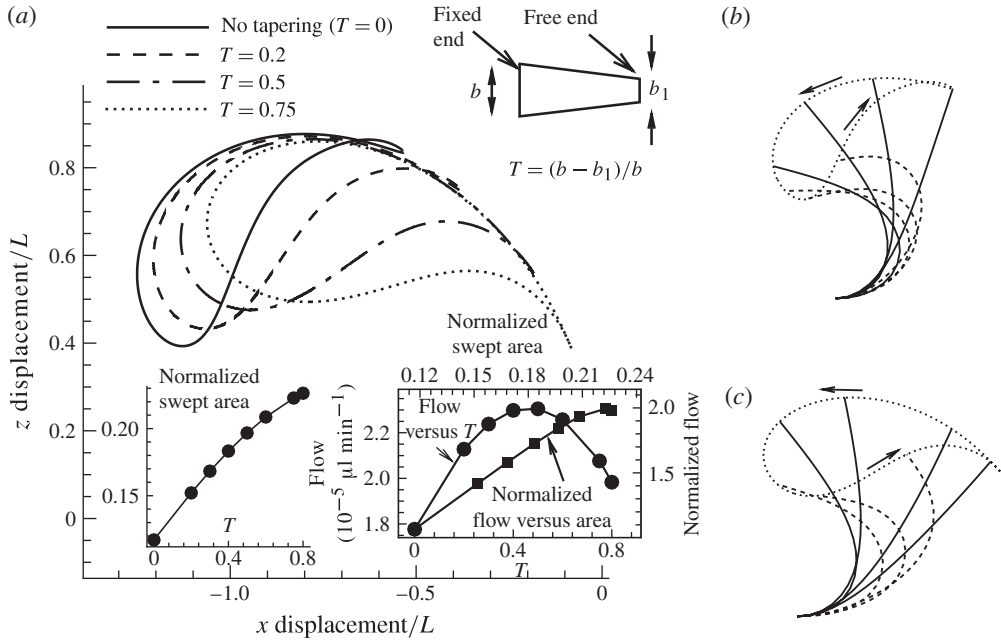
FIGURE 2. (*a*) Displacement of the cilia tip for different tapering in the width. The inset at the right shows the fluid flow (in microlitres per minute) for different values of tapering T, and the flow (normalized with $L^2(b_1 + b)/2$) as a function of the area swept (the area swept by the free end of the cilium, normalized with L^2) and the inset at the left shows the area swept normalized with (L^2) as a function of T. (*b,c*) Snapshots of the motion of the cilia in the x–z plane at different time instances for $T = 0$ and 0.5, respectively. The arrows show the direction of motion of the cilium, the dotted lines show the trajectory of the free end, the solid lines represent the cilium during the effective stroke and the dashed lines during the recovery stroke.

is triangular for a tapering T of unity. First, we find what value of T is required to generate an asymmetric motion. The trajectory of the tip of the cilium for different values of T is shown in figure 2(*a*). The area swept by the free end of the cilium increases when the tapering T is increased (see the left inset of figure 2*a*). Snapshots of the ciliary motion is shown in figure 2(*a,c*) for a $T = 0$ and 0.5, respectively.

The flow caused by the beating cilium is quantified by calculating the flux through the y–z plane and x–z plane. The far field velocity at a point in the fluid due to the nodal drag forces is given by (Blake 1972)

$$8\pi\mu u_i^f = \sum_{j=1}^{\text{nnod}} \frac{12d^j(r_i - r_i')(r_1 - r_1')(r_3 - r_3')}{|\boldsymbol{r} - \boldsymbol{r}'|^5} f_{f1}^j$$

$$+ \frac{12d^j(r_i - r_i')(r_2 - r_2')(r_3 - r_3')}{|\boldsymbol{r} - \boldsymbol{r}'|^5} f_{f2}^j + O\left(\frac{1}{|\boldsymbol{r}|^3}\right) \quad (3.1)$$

where $\boldsymbol{r}$ is the position of a point in the fluid and $\boldsymbol{r}'$ is the position of the node j, d^j is the distance between the node j and the no-slip plane, 'nnod' are the total number of nodes, f_{fk}^j represents the components of the point forces acting on the fluid at the jth node. In (3.1) Einstein's summation convention is used for repeated indices

with i taking the values 1, 2 and 3 which represent x, y and z directions, respectively; while k in f_{fk}^j takes the values 1 and 2 which represent x and y directions, respectively. The point forces can be obtained from $\boldsymbol{F}_f = \boldsymbol{K}_f \Delta \boldsymbol{P} / \Delta t$. The velocity flux in the x and y directions (Q_x and Q_y) are calculated by integrating the velocity in the x and y directions over the y–z and x–z planes, respectively:

$$Q_x = \int_0^\infty \int_{-\infty}^\infty u_x^f \, \mathrm{d}y \, \mathrm{d}z = \frac{1}{\pi\mu} \sum_{j=1}^{\mathrm{nnod}} d^j f_{fx}^j, \tag{3.2a}$$

$$Q_y = \int_0^\infty \int_{-\infty}^\infty u_y^f \, \mathrm{d}x \, \mathrm{d}z = \frac{1}{\pi\mu} \sum_{j=1}^{\mathrm{nnod}} d^j f_{fy}^j. \tag{3.2b}$$

This volume flux is integrated over the cycle to obtain the total volume flow during one cycle.

The volume flow per cycle (in microlitres per minute) for different values of tapering is shown in the right inset of figure 2(a). When the tapering is increased the area swept increases, whereas the area of the cilium which drives the flow decreases. Thus, the created flow is due to the competition between the swept area and the area of the cilium that pushes the fluid. As a result we see an initial increase of the flow, which reaches a maximum for a tapering T of 0.5, and then decreases. In the same inset, the fluid flow (normalized with $L^2(b_1 + b)/2$) is plotted as a function of the area swept (normalized with L^2) in the x–z plane. It is to be noted that normalizing the fluid flow with $(b_1 + b)/2$ gives the area flow per unit average width of the cilia, which on further normalization with L^2 becomes the normalized area flow. Hence, similar to the two-dimensional cases (Khaderi *et al.* 2009, 2010), the flow scales linearly with the swept area. Simulations were also performed for negative values of tapering (not shown), in which the width of the fixed end of a cilium is smaller than the free end. We found that for increasing values of negative tapering, the generated flow continues to decrease. For large values of negative tapering, the area swept by the tip of the cilia vanishes (they only oscillate symmetrically), resulting in zero flow.

To gain insight on the fluid propulsion, we look at the position of fluid particles which initially formed a plane parallel to the y–z plane for a cilium with a tapering T of 0.5, see figure 3. (At every time instant, the displacement of the fluid particles is calculated using their velocity (2.10). The new position is found by adding the displacement to their current position.) During the effective stroke, the cilium displaces the fluid particles in the negative x-direction (see figure 3a,c), after which the fluid particles are dragged back during the recovery stroke (see figure 3d,f). The displacement of the fluid particles can be observed by comparing the position of the particles in figure 3(a,f). The additional information, which we obtain from the three-dimensional model compared with the two-dimensional model, is the displacement of the fluid particles that are not present in the plane of beat.

3.2. *Effect of the cilia width and spacing*

We now examine the effect of the width and the cilia spacing on the flow generated by one row of cilia placed along the width. The geometry is shown in figure 4(a). We take n cilia of width b at the fixed edge whose tapering T is 0.5. The spacing between the cilia is p (the pitch), so that the total width occupied by the cilia row is np. For the simulations we choose $n = 4$ and calculate the flow created as a function of the
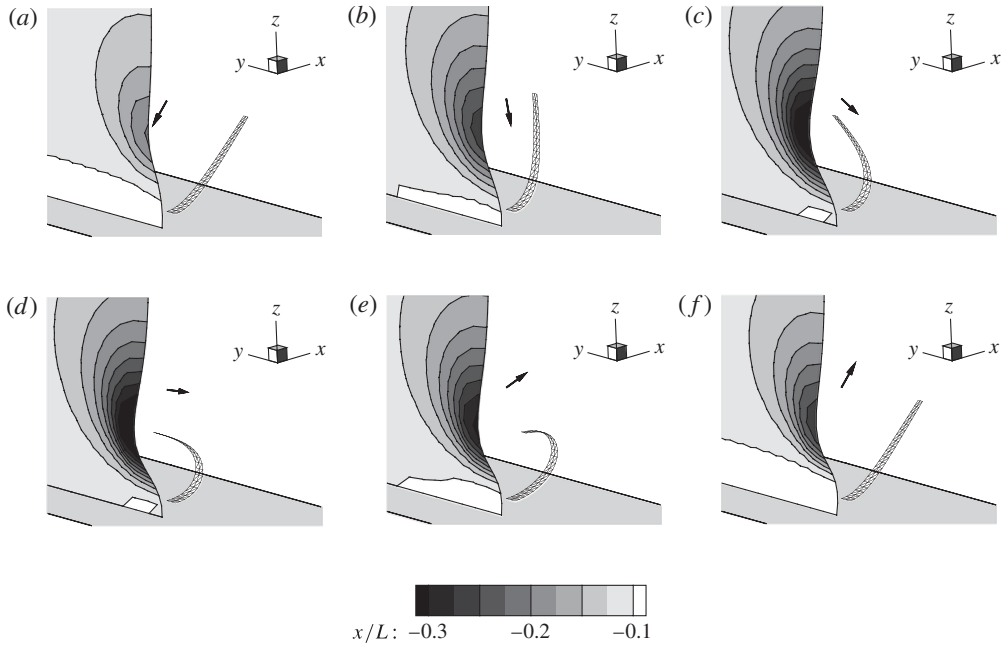
FIGURE 3. Snapshots of the motion of the cilium, beating in the x–z plane, at different instances of time for a representative cycle: (a–c) the effective strokes and (d–f) the recovery strokes. The evolving surface represents contours of the x coordinates of fluid particles which at time $t = 0$ were parallel to the y–z plane. During the effective stroke, the cilium displaces the fluid particles in the negative x-direction, and during the recovery stroke, the fluid particles are dragged back. The displacement of the fluid particles can be observed by comparing the position of the particles in (a,f): (a) Time $= 0$; (b) Time $= 0.15\,t_{ref}$; (c) Time $= 0.25\,t_{ref}$; (d) Time $= 0.325\,t_{ref}$; (e) Time $= 0.425\,t_{ref}$; (f) Time $= 0.5\,t_{ref}$.
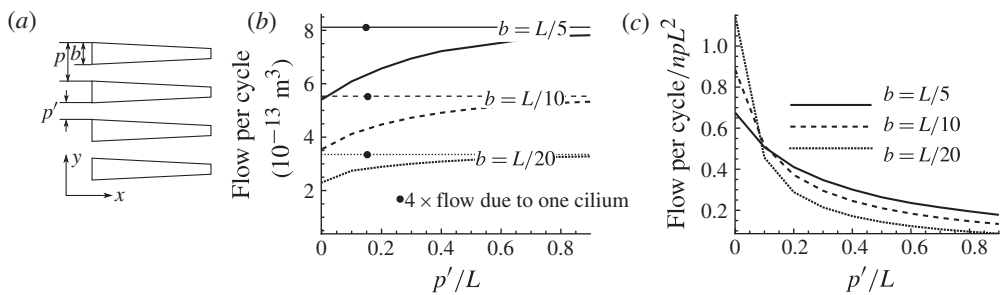

FIGURE 4. (a) Parameters used to study the effect of cilia spacing p' and width b for a given tapering. (b,c) Flow as a function of width and the pitch of the cilia spacing for cilia having a taper along the width.

spacing between the cilia $p' = p - b$. The spacing p' is varied from 0 (no spacing between the cilia at their fixed edge) to $0.9L$.

The horizontal lines in figure 4(b) represent four times the flow created by one cilium for different widths b. In the cases considered the increase of flow does not scale with the increase of the cilium width b. This suggests that the forces acting on
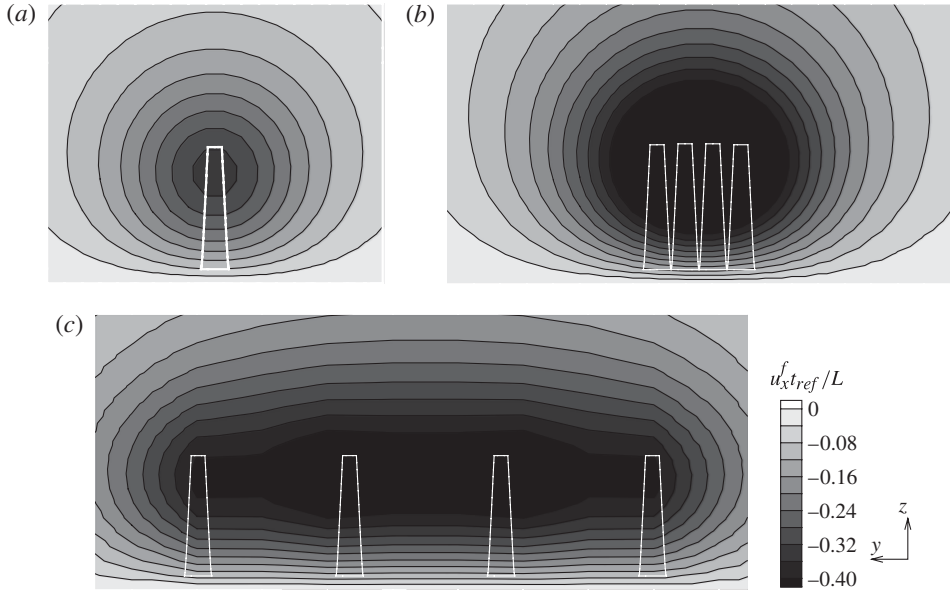
FIGURE 5. Front view (y–z plane) of the cilia at $t = t_{ref}/2$ (see figure 3f). The contours correspond to the fluid velocity in the x-direction on a plane parallel to y–z plane at a distance of 1.1L from the cilia fixed edge. The cilia influence a larger region of the fluid when the spacing is large, thus creating a larger flow as the spacing is increased: (*a*) $b = L/5$, $n = 1$; (*b*) $b = L/5$, $p' = 0$, $n = 4$; (*c*) $b = L/5$, $p' = 0.9L$, $n = 4$.

the fluid do not scale linearly with the cilia width b. Such a behaviour is also present in the case of ellipsoids (Happel & Brenner 1986).

The flow as a function of the spacing p' for various widths for $n = 4$ is also shown in figure 4(*b*). The flow created by the cilia is larger when they are further apart. The beating of a cilium imparts velocity to a small fluid region around it (see figure 5*a*). When four cilia are used, the region influenced by the cilia strongly depends on their spacing. When the spacing between them is small these regions overlap so that they collectively influence only a small region of the fluid, see figure 5(*b*). The total fluid region that can be influenced by the cilia increases as the spacing is increased (see figure 5*c*), reaching a maximum for spacings when the cilia do not hydrodynamically interact. In these cases, the flow converges to four times the flow caused by one cilium. This can also be rationalized from a force point of view. When the cilia are spaced closer together, they can move the fluid with less effort; this reduces the forces acting on the fluid due to the cilia motion. Consequently, the flow generated is low. A similar behaviour can also be seen in the case of two spheres which are translating at a given velocity (Happel & Brenner 1986). The force exerted by the spheres on the fluid is reduced when they are brought closer together.

A practically relevant question is: How much flow can the cilia generate per unit width? This question can be answered by normalizing the flow in figure 4(*b*) with the width of the cilia row (np). It can be seen that when the spacing p' is very low compared with the length L, the narrow cilia produce more flow; when the spacing is comparable to the length, the broader cilia create a higher flow. Note that for a given width, many narrow cilia spaced close together create the largest flow. Interestingly,
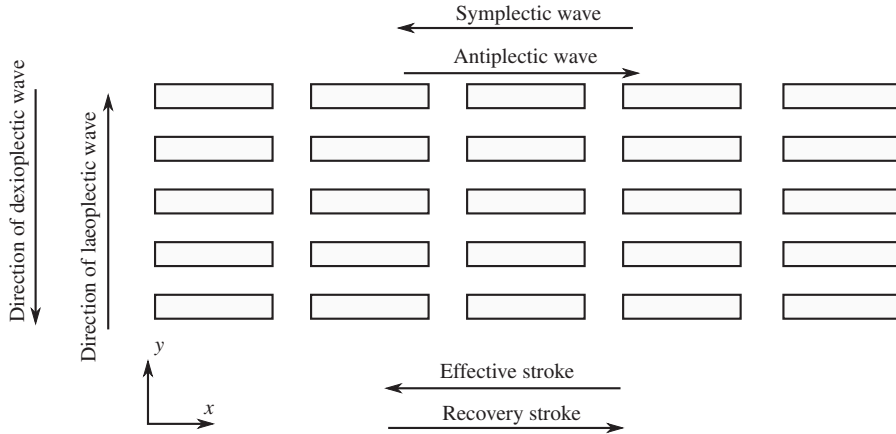
FIGURE 6. Schematic diagram showing the arrangement of cilia, the direction of effective and recovery strokes along with different kinds of metachronal waves.

this is the option chosen by nature. The natural cilia are hair-like structures that are spaced very close together.

3.3. *Effect of metachronal waves in the out-of-plane direction*

We now analyse the flow when an array of cilia move out-of-phase in the direction of their beat motion (antiplectic and symplectic metachrony) and in the direction orthogonal to it (laeoplectic and dexioplectic metachrony) (Childress 1981). In laeoplectic and dexioplectic metachrony, the effective stroke is to the left and right of the direction of propagation of the metachronal wave (see figure 6). To perform the simulations we choose five rows of cilia, with each row containing five cilia (see figure 6). A row refers to the arrangement of cilia in the y-direction. The cilia have a uniform width $b = 0.1L$ and a tapering in the thickness, such that the thickness of the cilia at the fixed end is 2 μm, which decreases linearly along the length to a thickness of 1 μm at the free end. The cilia spacings are $a = 1.1L$ (along the length) and $p = 0.2L$ (along the width). A rotating magnetic field with a magnitude of 20 mT is applied to every cilium at a frequency of 50 Hz. The phase difference in the magnetic field between adjacent cilia is varied from $\Delta\phi_x = -\pi/2$ to $\pi/2$ in the beat direction, and from 0 to $\Delta\phi_y = 2\pi/10$ in the direction normal to beat plane. The metachrony normal to the beat plane will create symmetric waves about $\Delta\phi_y = 0$. Hence, simulations are performed only for $\Delta\phi_y > 0$. A zero phase difference in any direction represents uniformly beating cilia in that direction, and a phase difference of $\pi/2$ represents the situation when adjacent cilia are in antiphase (standing wave). As the metachronal wave can also travel in a direction normal to the cilia beat, we also analyse the flow in this direction. In the following, the flow in the plane of the ciliary beat is referred to as primary flow and the flow normal to this plane is called secondary flow. The primary and secondary flow (normalized with $5bL^2$) are plotted as a function of the phase differences $\Delta\phi_x$ and $\Delta\phi_y$ in figure 7.

The flow is always larger for the cilia beating with antiplectic metachrony compared with synchronously beating cilia (in accordance with Khaderi *et al.* (2011*b*)). In the case of symplectic metachrony, the cilia obstruct the flow caused by their neighbours during the effective stroke (as also seen in the two-dimensional case
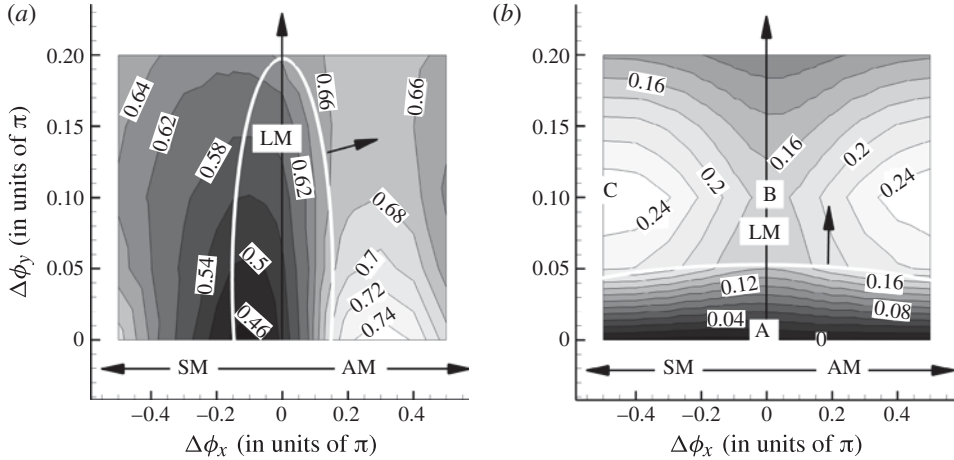
FIGURE 7. Primary and secondary flow created by cilia due to metachrony along and normal to the beat direction, respectively. The primary flow is larger when the cilia beat out of phase compared with synchronously beating cilia except for $-2\pi/10 < \Delta\phi_x < 0$ and $0 < \Delta\phi_y < \pi/10$. The secondary flow is created due to the plate-like motion of the rows of cilia, which reaches a maximum when the cilia motion between rows is antiphase and $\Delta\phi_y = \pi/10$. AM, SM and LM represent antiplectic, symplectic and laeoplectic metachrony, respectively. The velocity profiles for the set of phase differences corresponding to A, B and C are shown in figure 8: (*a*) primary flow; (*b*) secondary flow.

Gauger *et al.* (2009) and Khaderi *et al.* (2011*b*)). As a result, for antiplectic metachrony the flow is larger and for symplectic metachrony the flow is smaller than synchronously beating cilia, although the magnitude of increase is larger (for antiplectic metachrony) than the decrease (for symplectic metachrony). The flow obstruction is maximum for $-0.2\pi < \Delta\phi_x < 0$, in such cases the flow created is less than that created by synchronously beating cilia. In these cases, however, when $\Delta\phi_y > 0$ the decrease is lower because of the relaxation of the obstruction of positive flow. The flow exhibits a fluctuating behaviour only for the cases enclosed in the white curve, outside this region (in the direction of the arrow) the flow is unidirectional.

The laeoplectic metachrony creates a significant secondary flow (see figure 7*b*). To investigate the cause for the secondary flow, we look at the velocity created by two rows of cilia in the *y*-direction at the instance where the third cilium in each row of cilia is pointing towards the *z*-axis, see figure 8. In the cases (*a,b*) of figure 8, the cilia are exhibiting the effective stroke and are moving to the left. For synchronously beating cilia the velocity in the *y*-direction is symmetrically distributed (see figure 8*a*). Such a velocity distribution creates no net flux in the *y*-direction. However, when the cilia beat out of phase normal to the beat plane, the position of individual cilia leads to an asymmetric distribution of the *y*-velocity (see figure 8*b*). This asymmetry in the velocity profile is present at all *y*-positions and leads to a net flux in the *y*-direction.

The displacement of fluid particles initially near the rightmost row at different time instances is shown in figures 9 and 10 for cilia beating synchronously ($\Delta\phi_y = \Delta\phi_x = 0$) and out of phase ($\Delta\phi_y = \pi/10$ and $\Delta\phi_x = 0$), respectively. In the case of synchronously beating cilia, the symmetric velocity distribution about the *x*–*z* plane leads to a symmetric displacement of the particles throughout the cycle and
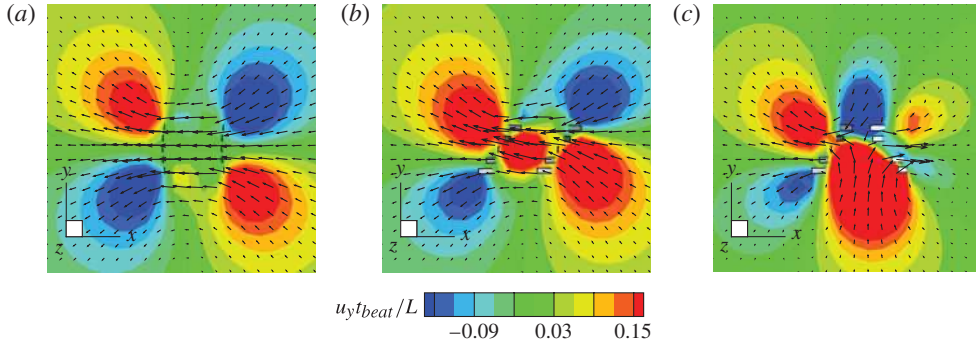
FIGURE 8. (Colour online) Velocity field for two rows of cilia beating (*a*) in phase; (*b*) out of phase in the *y*-direction and (*c*) out of phase in both the *x*- and *y*-directions. The contours represent the velocity in *y*-direction on a plane parallel to the *x*–*y* plane at a distance of $0.5L$ from the substrate. The arrows represent the velocity in the *x*–*y* plane. The velocity contours correspond to the set of phase differences marked by A, B and C in figure 7(*b*): (*a*) $\Delta\phi_x = \Delta\phi_y = 0$; (*b*) $\Delta\phi_x = 0$, $\Delta\phi_y = \pi/10$; (*c*) $\Delta\phi_x = \pi/2$, $\Delta\phi_y = \pi/10$.

leads to a net displacement only in the plane of the beat (*x*-direction). However, the asymmetric velocity distribution in the case of laeoplectic metachrony leads to an effective displacement of particles in the beat plane as well as in the *y*-direction, thereby creating the secondary flow.

When the cilia move in antiphase in the beat plane ($\Delta\phi_x \pm \pi/2$), the cilia in the adjacent rows move opposite to each other leading to large secondary flows for $\Delta\phi_y = \pi/10$ (see figure 7*b*). The velocity field at a particular instance is shown in figure 8(*c*), where the left row of cilia are exhibiting the effective stroke and the right row the recovery stroke. Such a motion of cilia creates a negative pressure between them that sucks in the fluid whose velocity has a prominent component in the *y*-direction (see figure 8*c*) and leads to a larger flux in the *y*-direction compared with cilia beating synchronously in the beat plane.

3.4. *Out-of-plane actuation of cilia*

In nature, the cilia on a Paramecium beat in a plane normal to the surface during the effective stroke, and during the recovery stroke they beat in a plane parallel to the surface. To achieve such a motion, we apply a magnetic field so that the magnetic field vector can be oriented in three-dimensional space (see figure 11). The dimensionless parameters take the following values. The magnetic number $M_n = 9.55$ (based on maximum field magnitude) and the fluid number $F_n = 0.06$ (based on $t_{beat} = 25$ ms).

Figure 12 shows the motion of a SPM cilium in which the cilium performs the effective stroke in the *x*–*z* plane and the recovery stroke in the *x*–*y* plane near the no-slip boundary. This results in large flow during the effective stroke and a small flow during the recovery stroke. The effective stroke consists of a uniform bending of the cilium in the *x*–*z* plane. During the recovery stroke, the cilium undergoes a significant amount of twisting, and comes back to the initial position (see figure 12*d–f*).

In figure 13(*a*), we show the flow as a function of the width of the cilium. It can be seen that flow drastically decreases as the width of the cilium is increased. This is because, the cilia can no longer twist and stay closer to the bottom boundary (see figure 13*b*). In such cases, we see a significant amount of flow during the recovery stroke, and this reduces the net amount of fluid propelled.
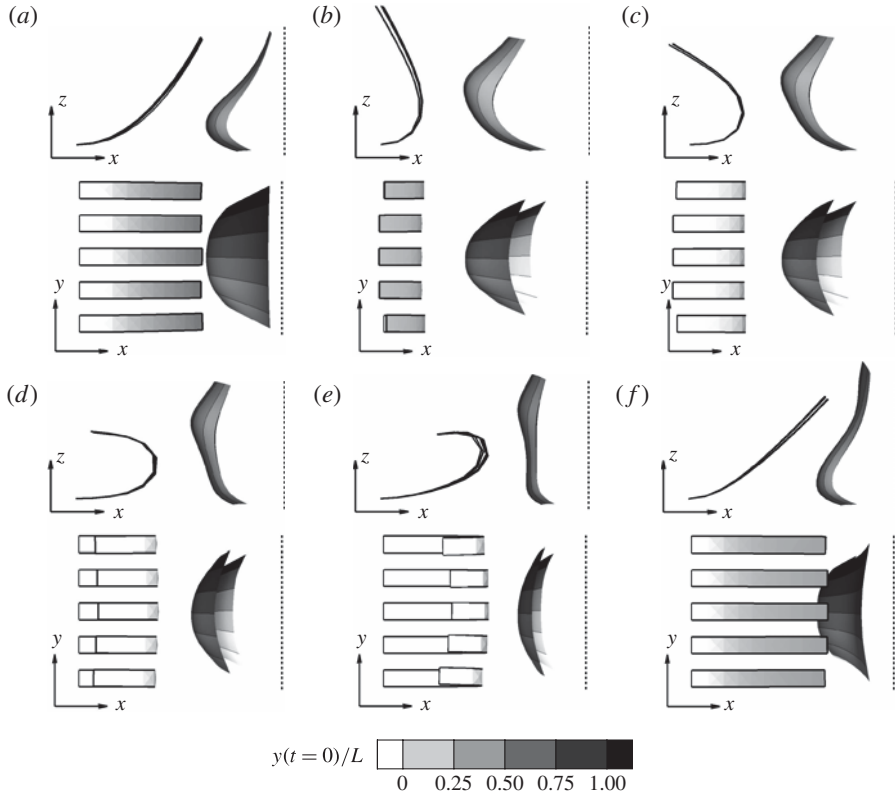
FIGURE 9. Synchronous motion ($\Delta\phi_y = \Delta\phi_x = 0$) of one row of cilia and the resulting motion of a plane of particles at different time instances. (*a*–*c*) Represents the front view and (*d*–*f*) represents the top view. The initial position of the particles plane in both the views is shown by the dashed lines. The particles move only in the plane of beat: (*a*) $t = 0.4t_{beat}$; (*b*) $t = 0.7t_{beat}$; (*c*) $t = 0.85t_{beat}$; (*d*) $t = 1.0t_{beat}$; (*e*) $t = 1.1t_{beat}$; (*f*) $t = 1.3t_{beat}$.

4. Summary

We have developed a FSI model to simulate the interaction of thin shells with the surrounding fluid. The shell structures are modelled using finite elements, while the fluid is modelled using boundary elements. The magnetic field is calculated from the magnetostatic boundary conditions. The developed model was used to simulate the flow due to magnetic artificial cilia, where it is shown that our model captures the essential physical phenomena governing the ciliary motion. Extensions of the present model include the implementation of a fast multipole method for the fluid model and implementing a boundary element method to calculate the local magnetic field in and around the cilia (Khaderi *et al.* 2009).

The three physical problems studied are the effect of: (i) cilia width and spacing; (ii) metachronal wave formation; and (iii) the out-of-plane actuation on the flow generated. It is found that the flow does not scale linearly with the width of the cilia, and for a given width, narrow and closely spaced cilia create the largest flow. A rectangular array of cilia were prescribed to beat with a metachronal motion in the direction of the width. When the cilia beat with the metachronal wave travelling along the width of the cilia, a flow is created in the direction of the effective stroke (primary flow)
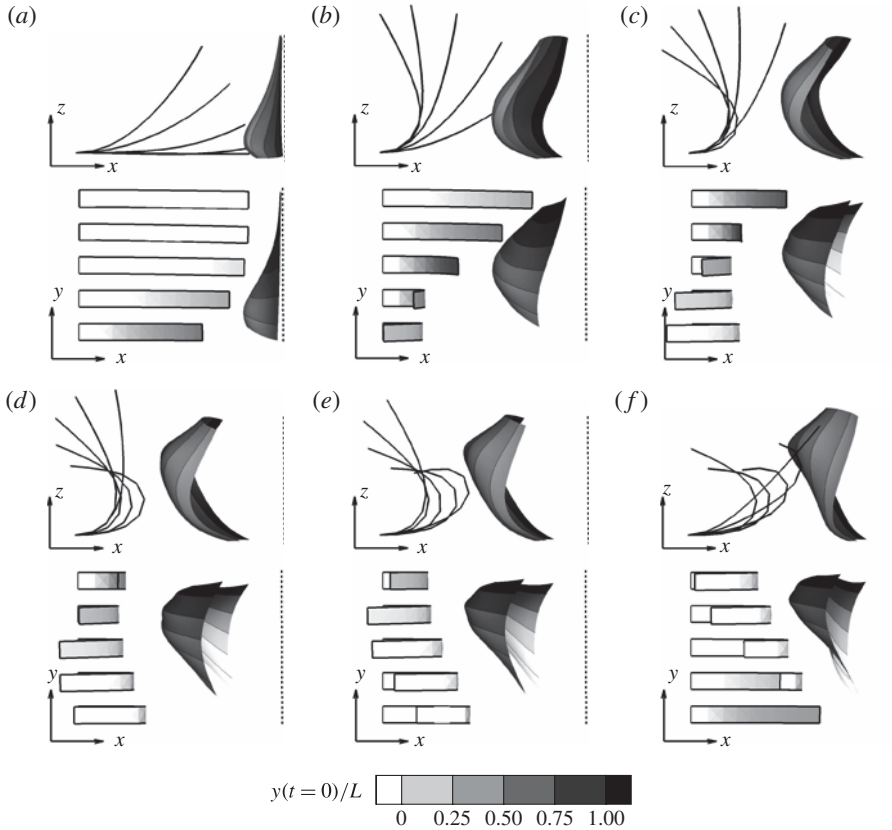
FIGURE 10. Out-of-phase motion ($\Delta\phi_y = \pi/10$ and $\Delta\phi_x = 0$) of one row of cilia and the resulting motion of a plane of particles at different time instances. (a–c) Represents the front view and (d–f) represents the top view. The initial position of the particle plane in both of the views is shown by the dashed lines. The particles move in the plane of beat and also orthogonal to the beat plane (compare instant (f) with figure 9f): (a) $t = 0.4t_{beat}$; (b) $t = 0.7t_{beat}$; (c) $t = 0.85t_{beat}$; (d) $t = 1.0t_{beat}$; (e) $t = 1.1t_{beat}$; (f) $t = 1.3t_{beat}$.

and due to the metachronal motion a significant flow is created in the direction of the cilia width (secondary flow). Subsequently, we analysed the generated flow due to a three-dimensional motion of the cilia, in which the effective stroke takes place in x–z plane and the recovery stroke takes place in the x–y plane. As the cilia undergo significant twisting during the recovery stroke, the motion of the cilia during the out-of-plane recovery stroke strongly depends on the cilia width. It is interesting to note that in case of laeoplectic metachrony of the cilia inside a microchannel, the primary flow will cause a net fluid transport, while the secondary flow can be used for the mixing of fluids.

Appendix A. Solid mechanics model

In this appendix we describe in detail the solid mechanics model used. Let the displacement of a point on the mid-surface be (u_0, v_0, w_0). As we model the cilia to be
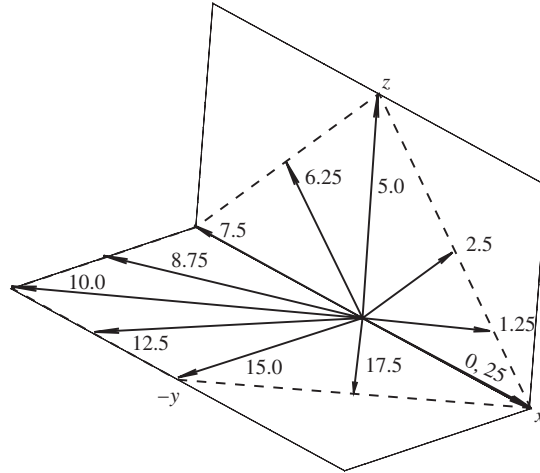
FIGURE 11. The arrows represent the applied magnetic field vector at different instances in time for a cilium to exhibit the effective stroke in the *x–z* plane and the recovery stroke in the *x–y* plane. The numbers adjacent to the arrows show the time in ms. The magnitude of the magnetic field at time instances 0, 5, 7.5 15 and 25 ms is 20 mT.
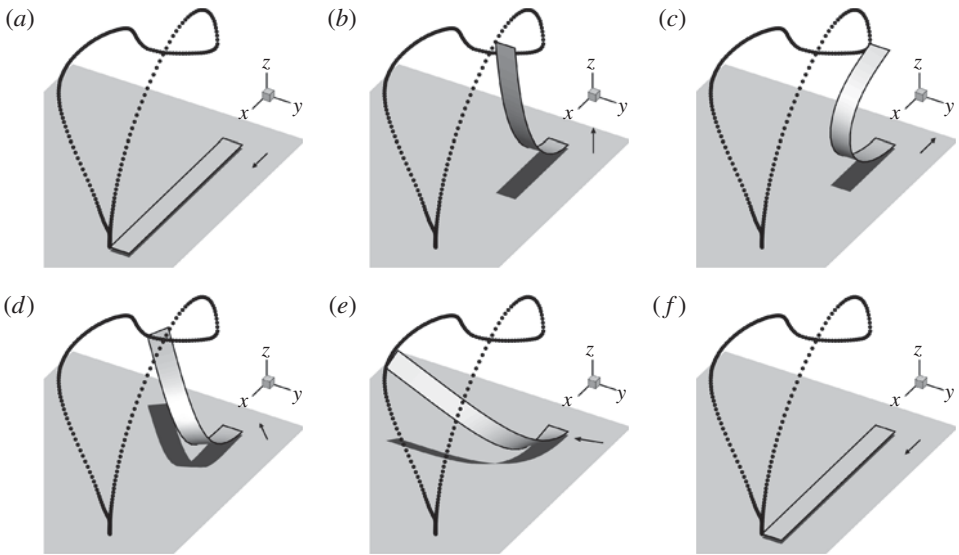

FIGURE 12. Snapshots of the motion of a SPM cilium due to a three-dimensional magnetic field. The arrow shows the applied magnetic field. The cilium performs the effective stroke in the *x–z* plane (see *a–c*) and the recovery stroke in the *x–y* plane (see *d–f*). Significant twisting of the cilium during the recovery stroke can be observed from the instances shown in (*d,e*).

shell structures, the displacement of any point on the normal is

$$u = u_0 + z\beta_x, \quad v = v_0 - z\beta_y, \quad w = w_0, \quad (A\,1)$$

where β_x and β_y are the rotations of the normal with respect to the *x*- and *y*-axes, respectively (see figure 14). Now, the only non-zero components of the
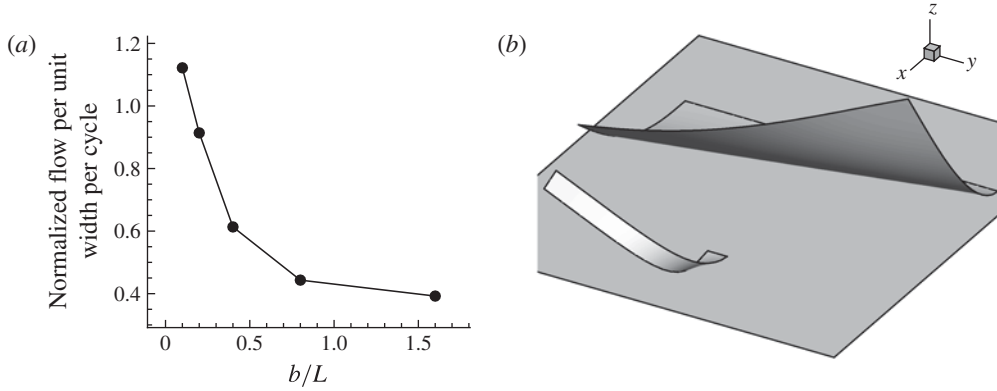
FIGURE 13. (*a*) Flow (normalized with L^2) due to the three-dimensional motion of a cilium (see figure 12) as a function of the width b/L (only one cilium is used in these simulations). The flow comes down drastically as the width b is increased. (*b*) Snapshots of two cilia of $b = L/10$ and $b = 1.6L$ when the cilia are half way through their recovery strokes (16 ms). The narrow cilium nicely twists, causing less flow during the recovery stroke.
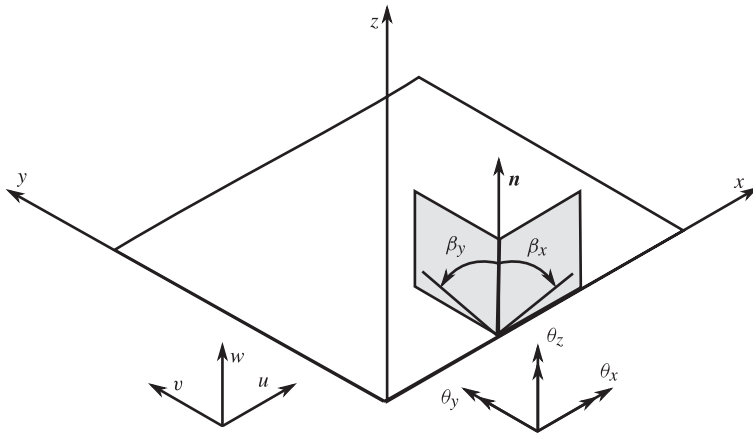

FIGURE 14. Schematic representation of the parameters involved in the shell element formulation.

Green–Lagrange strain are

$$\epsilon_x = \frac{\partial u}{\partial x} + \frac{1}{2}\left(\frac{\partial w}{\partial x}\right)^2, \quad \epsilon_y = \frac{\partial v}{\partial y} + \frac{1}{2}\left(\frac{\partial w}{\partial y}\right)^2, \quad 2\epsilon_{xy} = \frac{\partial u}{\partial y} + \frac{\partial v}{\partial x} + \frac{\partial w}{\partial x}\frac{\partial w}{\partial y}. \quad \text{(A 2)}$$

Taking the variation of the Green–Lagrange strain and substituting the displacements from (A 1), we get

$$\delta\epsilon_x = \frac{\partial \delta u}{\partial x} + \frac{\partial w}{\partial x}\frac{\partial \delta w}{\partial x} = \frac{\partial \delta u_0}{\partial x} + \frac{\partial w_0}{\partial x}\frac{\partial \delta w_0}{\partial x} + z\frac{\partial \delta \beta_x}{\partial x} = \delta\bar{\epsilon}_x + z\delta\kappa_x. \quad \text{(A 3)}$$

Similarly,

$$\delta\epsilon_y = \delta\bar{\epsilon}_y + z\delta\kappa_y \quad \text{and} \quad 2\delta\epsilon_{xy} = \delta\bar{\epsilon}_{xy} + z\delta\kappa_{xy}. \quad \text{(A 4)}$$

Here, $\kappa_x = \beta_{x,x}$, $\kappa_y = -\beta_{y,y}$ and $\kappa_{xy} = -\beta_{y,x} + \beta_{x,y}$ are the curvatures (consequently, the rotations in x–z plane and y–z plane are β_x and $-\beta_y$, respectively), and

$$\delta\bar{\epsilon}_x = \frac{\partial\delta u_0}{\partial x} + \frac{\partial w_0}{\partial x}\frac{\partial\delta w_0}{\partial x} = \frac{\partial\delta u_0}{\partial x} + \beta_x\delta\beta_x, \tag{A 5a}$$

$$\delta\bar{\epsilon}_y = \frac{\partial\delta v_0}{\partial y} + \frac{\partial w_0}{\partial y}\frac{\partial\delta w_0}{\partial y} = \frac{\partial\delta u_0}{\partial y} + \beta_y\delta\beta_y, \tag{A 5b}$$

and

$$\delta\bar{\epsilon}_{xy} = \frac{\partial\delta u_0}{\partial y} + \frac{\partial\delta v_0}{\partial x}\frac{\partial w_0}{\partial x}\frac{\partial\delta w_0}{\partial y} + \frac{\partial w_0}{\partial y}\frac{\partial\delta w_0}{\partial x} = \frac{\partial\delta u_0}{\partial y} + \frac{\partial\delta v_0}{\partial x} - \beta_x\delta\beta_y - \beta_y\delta\beta_x \tag{A 6}$$

are the membrane strains. The subscript $(\cdot)_{,x}$ denotes a partial derivative with respect to the x-direction. It is to be noted that the membrane strains contain terms which are linear in the in-plane displacements (u_0 and v_0), and nonlinear in the rotations.

The internal virtual work is

$$\delta W_{int} = \int_{V_0} (\sigma_x\delta\epsilon_x + \sigma_y\delta\epsilon_y + 2\sigma_{xy}\delta\epsilon_{xy})\,\mathrm{d}V_0, \tag{A 7}$$

where σ_x, σ_y and σ_{xy} are the components of the second Piola–Kichhoff stress tensor and $\mathrm{d}V_0$ represents an elemental volume in the undeformed configuration. By using the definitions of membrane strains and curvatures, the internal virtual work can be written as

$$\delta W_{int} = \int_{A_0} (\delta\boldsymbol{\epsilon}\cdot\boldsymbol{P} + \delta\boldsymbol{\kappa}\cdot\boldsymbol{M})\,\mathrm{d}A_0, \tag{A 8}$$

where $\boldsymbol{\kappa} = [\kappa_x\ \kappa_y\ \kappa_{xy}]^{\mathrm{T}}$, $\boldsymbol{\epsilon} = [\bar{\epsilon}_x\ \bar{\epsilon}_y\ \bar{\epsilon}_{xy}]^{\mathrm{T}}$, $\mathrm{d}A_0$ represents an elemental area in the undeformed configuration,

$$\boldsymbol{P} = \begin{Bmatrix} P_x \\ P_y \\ P_{xy} \end{Bmatrix} = \frac{hE}{1-\nu^2}\begin{bmatrix} 1 & -\nu & 0 \\ -\nu & 1 & 0 \\ 0 & 0 & \dfrac{1-\nu}{2} \end{bmatrix}\begin{Bmatrix} \bar{\epsilon}_x \\ \bar{\epsilon}_y \\ \bar{\epsilon}_{xy} \end{Bmatrix} = \boldsymbol{D}^M\boldsymbol{\epsilon}, \tag{A 9}$$

and

$$\boldsymbol{M} = \begin{Bmatrix} M_x \\ M_y \\ M_{xy} \end{Bmatrix} = \frac{h^3E}{12(1-\nu^2)}\begin{bmatrix} 1 & -\nu & 0 \\ -\nu & 1 & 0 \\ 0 & 0 & \dfrac{1-\nu}{2} \end{bmatrix}\begin{Bmatrix} \kappa_x \\ \kappa_y \\ \kappa_{xy} \end{Bmatrix} = \boldsymbol{D}^B\boldsymbol{\kappa}, \tag{A 10}$$

with h being the thickness of the shell element, E the elastic modulus and ν the Poisson's ratio. In (A 8), the first and second terms represent the virtual work done by the membrane forces and bending moments, respectively. The internal virtual work at time $t + \Delta t$ is

$$\delta W_{int}^{t+\Delta t} = \int_{A_0} (\delta\boldsymbol{\epsilon}^{t+\Delta t}\cdot\boldsymbol{P}^{t+\Delta t} + \delta\boldsymbol{\kappa}^{t+\Delta t}\cdot\boldsymbol{M}^{t+\Delta t})\,\mathrm{d}A_0. \tag{A 11}$$

Expanding this equation linearly in time yields:

$$\delta W_{int}^{t+\Delta t} = \int_{A_0} ((\delta \epsilon^t + \Delta \delta \epsilon) \cdot (P^t + \Delta P) + (\delta \kappa^t + \Delta \delta \kappa) \cdot (M^t + \Delta M)) \, dA_0,$$

$$= \int_{A_0} (\delta \epsilon^t \cdot P^t + \delta \kappa^t \cdot M^t + \Delta \delta \epsilon \cdot P^t + \delta \epsilon^t \cdot \Delta P + \delta \kappa^t \cdot \Delta M) \, dA_0. \quad (A\,12)$$

In the last equation, the higher-order terms are neglected and use has been made of the fact that $\Delta \delta \kappa = 0$.

We discretize (A 12) using three-node triangular finite elements. Each element has three displacement u, v, w and three rotational degrees of freedom $\theta_x, \theta_y, \theta_z$ at each node. The nodal displacement vector for each element has 18 degrees of freedom and is written as

$$p = [u_1 \ v_1 \ w_1 \ \theta_{x1} \ \theta_{y1} \ \theta_{z1} \ u_2 \ v_2 \ w_2 \ \theta_{x2} \ \theta_{y2} \ \theta_{z2} \ u_3 \ v_3 \ w_3 \ \theta_{x3} \ \theta_{y3} \ \theta_{z3}]^T. \quad (A\,13)$$

The rotations of the normal (β_x and β_y) are interpolated using the discrete Kirchhoff formulation: $\beta_x = H_{xp}$ and $\beta_y = H_{yp}$ and the variation of the curvature is related to the nodal displacement vector as

$$\delta \kappa = C \delta p. \quad (A\,14)$$

The forms of H_x, H_y and C are given by Batoz *et al.* (1980). The variation of the membrane strains can be written using the DKTs for the nonlinear part and CSTs with drilling degrees of freedom for the linear part. This gives

$$\delta \epsilon = \begin{Bmatrix} \bar{\epsilon}_x \\ \bar{\epsilon}_y \\ \bar{\epsilon}_{xy} \end{Bmatrix}$$

$$= \begin{bmatrix} 1 & y & 0 & 0 & 0 \\ 0 & 0 & 1 & x & 0 \\ 0 & -x & 0 & -y & 1 \end{bmatrix} B_1 \delta p + \begin{bmatrix} p^T H_x{}^T H_x \\ p^T H_y{}^T H_y \\ p^T (-H_y{}^T H_x - H_x{}^T H_y) \end{bmatrix} \delta p,$$

$$= (B_L + B_{NL}) \delta p. \quad (A\,15)$$

Here B_1 is a matrix which depends on the coordinates of the vertices of the triangle whose form can be found elsewhere (Allman 1984). Now, the increment of the virtual strain is given by

$$\Delta \delta \epsilon = [\Delta p^T H_x{}^T H_x, \ \Delta p^T H_y{}^T H_y, \ \Delta p^T (-H_y^T H_x - H_x{}^T H_y)]^T \delta p. \quad (A\,16)$$

The internal virtual work (equation (A 12)) can be now written in terms of the interpolation matrices (using (A 14), (A 15) and (A 16)) as

$$\delta W_{int}^{t+\Delta t} = \int_{A_0} [\delta p^T (B_L{}^T + B_{NL}{}^T) P^t + \delta p^T C^T M^t$$

$$+ \delta p^T (H_x{}^T H_x P_x^t + H_y{}^T H_y P_y^t - (H_x{}^T H_y + H_x{}^T H_y) P_{xy}^t) \Delta p$$

$$+ \delta p^T (B_L{}^T + B_{NL}{}^T) D^M (B_L + B_{NL}) \Delta p + \delta p^T C^T D^B C \Delta p] \, dA_0. \quad (A\,17)$$

We now adopt an updated Lagrangian point of view and choose the domain of integration to be the deformed configuration. This makes the total displacements p to

be zero so that $\boldsymbol{B}_{NL}$ vanishes. The internal virtual work now becomes

$$\delta W_{int}^{t+\Delta t} = \delta \boldsymbol{p}^{\mathrm{T}} \boldsymbol{f}_{int}^{t} + \delta \boldsymbol{p}^{\mathrm{T}} (\boldsymbol{k}_M + \boldsymbol{k}_G) \Delta \boldsymbol{p}, \tag{A 18}$$

where

$$\boldsymbol{f}_{int}^{t} = \int_{A} (\boldsymbol{B}_{L}^{\mathrm{T}} \boldsymbol{P}^{t} + \boldsymbol{C}^{\mathrm{T}} \boldsymbol{M}^{t}) \, \mathrm{d}A \tag{A 19}$$

is the internal force vector,

$$\boldsymbol{k}_M = \int_{A} (\boldsymbol{B}_{L}^{\mathrm{T}} \boldsymbol{D}^{M} \boldsymbol{B}_{L} + \boldsymbol{C}^{\mathrm{T}} \boldsymbol{D}^{B} \boldsymbol{C}) \, \mathrm{d}A \tag{A 20}$$

is the material stiffness matrix and

$$\boldsymbol{k}_G = \int_{A} (\boldsymbol{H}_x^{\mathrm{T}} \boldsymbol{H}_x P_x^t + \boldsymbol{H}_y^{\mathrm{T}} \boldsymbol{H}_y P_y^t - (\boldsymbol{H}_x^{\mathrm{T}} \boldsymbol{H}_y + \boldsymbol{H}_x^{\mathrm{T}} \boldsymbol{H}_y) P_{xy}^t) \, \mathrm{d}A \tag{A 21}$$

is the geometric stiffness matrix.

The internal virtual work in (equation (A 18)) is in the local coordinates. This equation after transforming to the global coordinates (Zienkiewicz & Taylor 2002) and performing the standard finite-element assembly can be written as

$$\delta W_{int}^{t+\Delta t} = \delta \boldsymbol{P}^{\mathrm{T}} \boldsymbol{F}_{int}^{t} + \delta \boldsymbol{P}^{\mathrm{T}} (\boldsymbol{K}_M + \boldsymbol{K}_G) \Delta \boldsymbol{P}, \tag{A 22}$$

where $\boldsymbol{P}$ is the global displacement vector.

The external work at time $t + \Delta t$ due to body forces and body moments can be written as

$$\delta W_{ext}^{t+\Delta t} = \int_{V} (f_x \delta u + f_y \delta v + f_z \delta w - N_x \delta \beta_y + N_y \delta \beta_x) \, \mathrm{d}V, \tag{A 23}$$

where f_x, f_y and f_z are the body forces and N_x and N_y are the body moments. Because the current shell element does not provide an interpolation function for the in-plane rotations, they are incorporated using equivalent point forces acting at the nodes of an element. For the external virtual work, we choose to interpolate the translational displacement using linear shape functions, and for the rotations we use the shape functions from the DKTs:

$$\delta W_{ext}^{t+\Delta t} = \delta \boldsymbol{p}^{\mathrm{T}} \int_{V} (\boldsymbol{N}^{\mathrm{T}} [f_x \, f_y \, f_z]^{\mathrm{T}} - \boldsymbol{H}_y^{\mathrm{T}} N_x + \boldsymbol{H}_x^{\mathrm{T}} N_y) \, \mathrm{d}V = \delta \boldsymbol{p}^{\mathrm{T}} \boldsymbol{f}_{ext}^{t+\Delta t}, \tag{A 24}$$

where

$$\boldsymbol{N} = \begin{bmatrix} N_1 & 0 & 0 & 0 & 0 & 0 & N_2 & 0 & 0 & 0 & 0 & 0 & N_3 & 0 & 0 & 0 & 0 & 0 \\ 0 & N_1 & 0 & 0 & 0 & 0 & 0 & N_2 & 0 & 0 & 0 & 0 & 0 & N_3 & 0 & 0 & 0 & 0 \\ 0 & 0 & N_1 & 0 & 0 & 0 & 0 & 0 & N_2 & 0 & 0 & 0 & 0 & 0 & N_3 & 0 & 0 & 0 \end{bmatrix}, \tag{A 25}$$

N_1, N_2 and N_3 are the standard area coordinates of a three-node triangular element (Zienkiewicz & Taylor 2002). After performing the standard finite-element assembly procedure, the external virtual work can be written as

$$\delta W_{ext}^{t+\Delta t} = \delta \boldsymbol{P}^{\mathrm{T}} \boldsymbol{F}_{ext}^{t+\Delta t}. \tag{A 26}$$

Appendix B. Benchmark tests for the solid mechanics model

The three-dimensional numerical model is benchmarked using three reference problems: (i) nonlinear deflection of a square clamped plate (Hughes & Liu 1981);
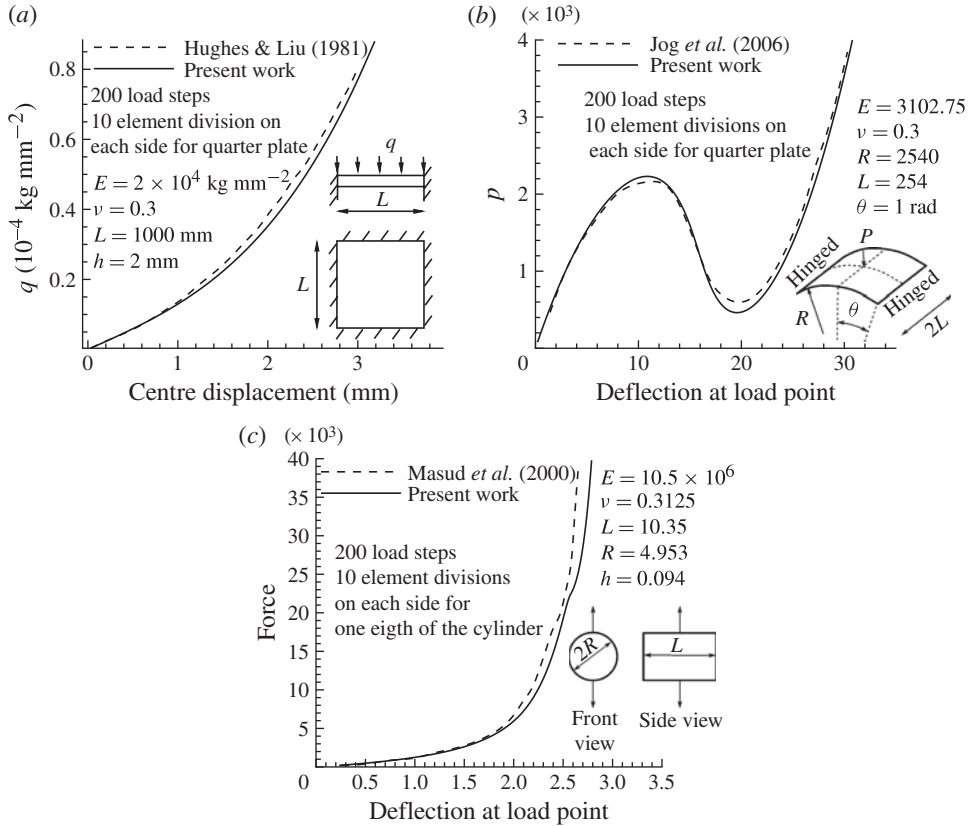
FIGURE 15. Benchmark tests for the shell element. (*a*) Load-deflection curve for the clamped square plate subjected to a uniform pressure on its surface, compared against (Hughes & Liu 1981). (*b*) Load-deflection curve for the hinged cylindrical roof subjected to a point load at the centre, compared with Jog & Kelkar (2006). (*c*) Load-deflection curve for the pinched cylinder problem, compared with Masud *et al.* (2000).

(ii) deflection of a hinged cylindrical roof (Jog & Kelkar 2006); and (iii) pinching of an open-ended cylinder (Masud, Tham & Liu 2000). All of the problems analysed possess a significant amount of nonlinearity. The tests have been performed with a fixed load increment. Symmetries present in the problems have been used to reduce the time for computations. The results plotted in figure 15 show that the shell element formulation is in good agreement with the results available in the literature.

Appendix C. Benchmark tests for the fluid dynamic model

To benchmark the fluid dynamic model we choose the problem of the translation of a sphere near a no-slip surface. This problem was also solved numerically using the method of regularized Stokeslets (Ainley *et al.* 2008). The analytical values of the forces (per unit velocity) when the sphere translates parallel and perpendicular to the no-slip boundary are 2.6475 and 23.6605 (in units of $6\pi\mu r\upsilon$), respectively. The spacing between the sphere and the no-slip plane is very small compared with the radius of the sphere r (0.0453r). This results in a large velocity gradient between the sphere and the no-slip plane. The singular and non-singular integrals encountered
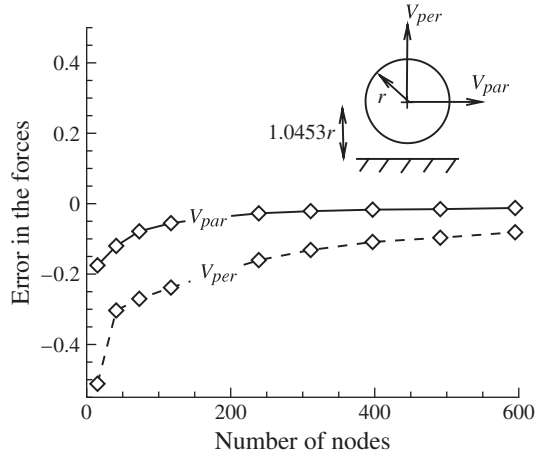
FIGURE 16. A sphere translating parallel/perpendicular to the wall: error in the forces as a function of the number of nodes used to discretize sphere.

during the integration of (2.10) are integrated using 36 and 7 gauss points, respectively (Pozrikidis 2002). For comparison we use the same discretization as that of (Ainley *et al.* 2008); the surface of the sphere is covered with equally spaced points using a spherical coordinate system and then triangulated.

The error in the forces are plotted as a function of the number of nodes used to discretize the sphere, see figure 16. The convergence is slow in the case when the sphere translates perpendicular to the wall. However, the convergence obtained from our method is much better than that obtained in (Ainley *et al.* 2008). The sphere was discretized into 2718 points for an error of 11 % in the perpendicular force compared to 400 points in our case.

Appendix D. Benchmark test for the FSI model

As benchmark tests for the FSI models are not available in the literature, we use a two-dimensional FSI model (Khaderi *et al.* 2009) to validate the present formulation. The problem chosen is the relaxation of a plate of length L, width b and thickness h subjected to an initial displacement. The plate is placed parallel to the no-slip plane at a distance of $0.1L$, see figure 17(*a*). The elastic modulus of the plate is taken to be 1 MPa, and the viscosity of the fluid is taken to 1 mPa s. The plate is clamped along its width, while the corresponding opposite edge of the plate is given an initial transverse displacement of $0.25L$ in the direction opposite to the no-slip plane, and is released at time $t = 0$. The geometry and boundary conditions for the two-dimensional model are shown in figure 17(*b*). The response of the plate as a function of time, for different widths of the plate in the direction normal to the plane of its motion, is shown in figure 18. It can be seen that as the width of the plate increases the response of the three-dimensional model converges to the two-dimensional model. The beam in the two-dimensional model is discretized into 80 elements. The plate element is divided into 12 elements along L and into $12b/L$ elements along b. The 36 and 7 gauss points were used to integrate the singular integral and non-singular integrals, respectively.
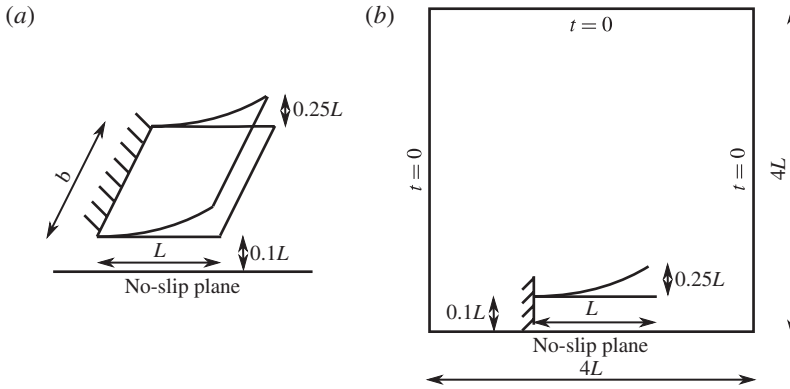
FIGURE 17. Benchmark test for the FSI problem. (*a*) Schematic representation of the geometry used to benchmark the three-dimensional model. (*b*) The two-dimensional model.
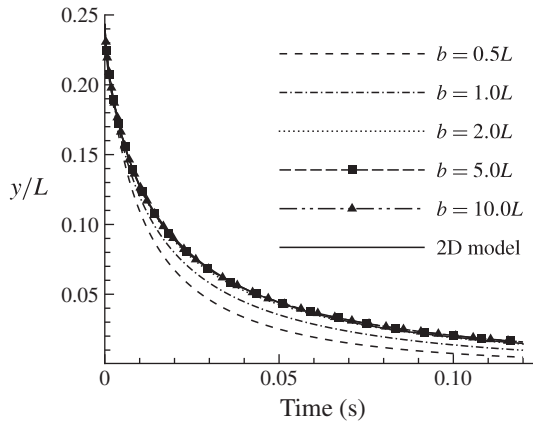

FIGURE 18. Benchmark test for the FSI problem. Comparison of relaxation of a plate subjected to an initial displacement of the free end with the two-dimensional model.

Appendix E. Benchmarking the magneto-static model

We use the previously developed two-dimensional magneto-mechanical model (Khaderi *et al.* 2009) to benchmark the magneto-mechanical model presented in § 2.4. To this end we subject a magnetic cilium to an external magnetic field, and compare the tip displacement resulting from the two-dimensional model (Khaderi *et al.* 2009) with the tip displacement obtained from the present model. We would like to remind the reader that in the two-dimensional case, the magnetic field is calculated by solving the Maxwell's equations. We take the case of a SPM cilium which is tapered in the thickness direction and subject it to a rotating magnetic field of $B_0 = 20$ mT with a time period of 20 ms. The length L of the film is 100 μm, the thickness h is 2 μm at the fixed end and decreases uniformly along the length, so that the thickness at the free end is 1 μm. The width of the cilium b is taken to be $2L$ (when $b > 2L$ the three-dimensional model converges to the two-dimensional model, see § D). The elastic modulus of the cilium is taken to be 1 MPa. The tip displacements are compared
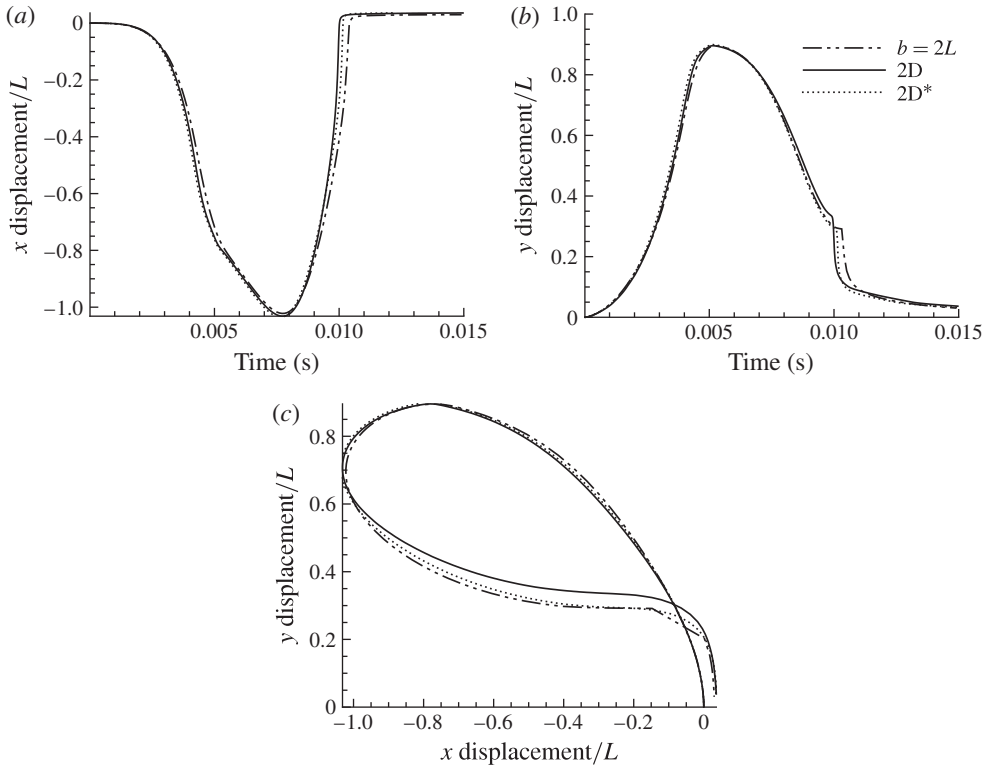
FIGURE 19. Cilium tip displacement computed by solving the Maxwell's equations in a two-dimensional model (solid lines) and by using the magneto-static boundary conditions for the three-dimensional model with $b = 2L$ (broken lines). Dotted lines represent the results from the two-dimensional model, with the magnetic field calculated using the magneto-static boundary conditions.

in figure 19. We see that the tip displacement resulting from the present model is in good agreement with the displacement computed by the two-dimensional model in which the magnetic field is obtained from the solution of Maxwell's equations. The discrepancy between the approaches results from two sources. The fluid–solid coupling and the way the magnetic fields are calculated. To show that the error due to the fluid–solid coupling is low, we also plot the displacement of the tip of the cilium for the two-dimensional case with the magnetic fields calculated from the magneto-static boundary conditions similar to the three-dimensional model, see the dotted lines in figure 19. It can be seen that the error in the solid–fluid coupling is indeed small and the main difference comes from the way the magnetic fields are calculated.

REFERENCES

AINLEY, J., DURKIN, S., EMBID, R., BOINDALA, P. & CORTEZ, R. 2008 The method of images for regularized stokeslets. *J. Comput. Phys.* **227** (9), 4600–4616.

ALLMAN, D. J. 1984 A compatible triangular element including vertex rotations for plane elasticity analysis. *Comput. Struct.* **19** (1–2), 1–8 (special memorial issue).

BATHE, K. J. & HO, L. W. 1981 A simple and effective element for analysis of general shell structures. *Comput. Struct.* **13** (5–6), 673–681.

BATOZ, J. L., BATHE, K. J. & HO, L. W. 1980 A study of three-node triangular plate bending elements. *Intl J. Numer. Meth. Engng* **15**, 1771–1812.

BELARDI, J., SCHORR, N., PRUCKER, O. & RUHE, J. 2011 Artificial cilia: generation of magnetic actuators in microfluidic systems. *Adv. Funct. Mater.* **21**, 3314–3320.

BLAKE, J. R. 1971 A note on the image system for a Stokeslet in a no-slip boundary. *Math. Proc. Cambridge Phil. Soc.* **70** (02), 303–310.

BLAKE, J. R. 1972 A model for the micro-structure in ciliated organisms. *J. Fluid Mech.* **55** (01), 1–23.

CHEN, Z. S., HOFSTETTER, G. & MANG, H. A. 1998 A Galerkin-type Be–Fe formulation for elasto-acoustic coupling. *Comput. Meth. Appl. Mech. Engng* **152** (1–2), 147–155 (containing papers presented at the symposium on Advances in Computational Mechanics).

CHILDRESS, S. 1981 *Mechanics of Swimming and Flying*. Cambridge University Press.

DONEA, J., GIULIANI, S. & HALLEUX, J. P. 1982 An arbitrary Lagrangian–Eulerian finite element method for transient dynamic fluid–structure interactions. *Comput. Meth. Appl. Mech. Engng* **33** (1–3), 689–723.

FAHRNI, F., PRINS, M. W. J. & VAN IJZENDOORN, L. J. 2009 Micro-fluidic actuation using magnetic artificial cilia. *Lab on a Chip* **9**, 3413–3421.

FULFORD, G. R. & BLAKE, J. R 1986 Muco-ciliary transport in the lung. *J. Theor. Biol.* **121** (4), 381–402.

GAUGER, E. M., DOWNTON, M. T. & STARK, H. 2009 Fluid transport at low Reynolds number with magnetically actuated artificial cilia. *Eur. Phys. J.* E **28**, 231–242.

GERSTENBERGER, A. & WALL, W. A. 2008 An extended finite element method/Lagrange multiplier based approach for fluid–structure interaction. *Comput. Meth. Appl. Mech. Engng* **197** (19–20), 1699–1714 (computational methods in fluid–structure interaction).

GERSTENBERGER, A. & WALL, W. A 2010 An embedded Dirichlet formulation for 3d continua. *Intl J. Numer. Meth. Engng* **82** (5), 537–563.

HAPPEL, J. & BRENNER, H. 1986 *Low Reynolds Number Hydrodynamics: with Special Applications to Particulate Media*. Martinus Nijhoff.

HUGHES, T. J. R. & LIU, W. K. 1981 Nonlinear finite element analysis of shells: Part I. Three-dimensional shells. *Comput. Meth. Appl. Mech. Engng* **26** (3), 331–362.

HUSSONG, J., SCHORR, N., BELARDI, J., PRUCKER, O., RUHE, J. & WESTERWEEL, J. 2011 Experimental investigation of the flow induced by artifiial cilia. *Lab on a Chip* **11**, 2017–2022.

JOG, C. S. & KELKAR, P. P. 2006 Non-linear analysis of structures using high performance hybrid elements. *Intl J. Numer. Meth. Engng* **68**, 473–501.

KHADERI, S. N., BALTUSSEN, M. G. H. M., ANDERSON, P. D., IOAN, D., DEN TOONDER, J. M. J. & ONCK, P. R. 2009 Nature-inspired microfluidic propulsion using magnetic actuation. *Phys. Rev.* E **79** (4), 046304.

KHADERI, S. N., BALTUSSEN, M. G. H. M., ANDERSON, P. D., DEN TOONDER, J. M. J. & ONCK, P. R. 2010 The breaking of symmetry in microfluidic propulsion driven by artificial cilia. *Phys. Rev.* E **82**, 027302.

KHADERI, S. N., CRAUS, C. B., HUSSONG, J., SCHORR, N., BELARDI, J., WESTERWEEL, J., PRUCKER, O., RUHE, J., DEN TOONDER, J. M. J. & ONCK, P. R. 2011*a* Magnetically-actuated artificial cilia for microfluidic propulsion. *Lab on a Chip* **11**, 2002–2010.

KHADERI, S. N., DEN TOONDER, J. M. J. & ONCK, P. R. 2011*b* Microfluidic propulsion by the metachronal beating of magnetic artificial cilia: a numerical analysis. *J. Fluid Mech.* **688**, 44–65.

LASER, D. J & SANTIAGO, J. G 2004 A review of micropumps. *J. Micromech. Microengng* **14** (6), R35–R64.

VAN LOON, R., ANDERSON, P. D. & VAN DE VOSSE, F. N. 2006 A fluid–structure interaction method with solid-rigid contact for heart valve dynamics. *J. Comput. Phys.* **217**, 806–823.

MASUD, A., THAM, C. L. & LIU, W. K. 2000 A stabilized 3-d co-rotational formulation for geometrically nonlinear analysis of multi-layered composite shells. *Comput. Mech.* **26**, 1–12.

VAN OOSTEN, C. L., BASTIAANSEN, C. W. M. & BROER, D. J. 2009 Printed artificial cilia from liquid-crystal network actuators modularly driven by light. *Nat. Mater.* **8**, 677–682.

PESKIN, C. S. 2002 The immersed boundary method. *Acta Numerica* **11** (-1), 479–517.

POZRIKIDIS, C. 2002 *A Practical Guide to Boundary Element Methods*. Chapman & Hall/CRC.

SALSAC, A. V., BIESEL, D. B. & TALLEC, P. L. 2010 Coupling of finite element and boundary integral methods for a capsule in a Stokes flow. *Intl J. Numer. Meth. Engng* 829–850.

SCHNEIDER, S. 2008 Fe/fmbe coupling to model fluidstructure interaction. *Intl J. Numer. Meth. Engng* 2137–2156.

DEN TOONDER, J., BOS, F., BROER, D., FILIPPINI, L., GILLIES, M., DE GOEDE, J., MOL, T., REIJME, M., TALEN, W., WILDERBEEK, H., KHATAVKAR, V. & ANDERSON, P. 2008 Artificial cilia for active micro-fluidic mixing. *Lab on a Chip* **8** (4), 533–541.

ZIENKIEWICZ, O. C. & TAYLOR, R. L. 2002 *The Finite Element Method*. Butterworth-Heinemann.